THE JOURNAL OF BIOLOGICAL CHEMISTRY VOL. 282, NO. 6, pp. 4124–4135, February 9, 2007

Combined Deletion of Mouse Dematin-Headpiece and β-Adducin Exerts a Novel Effect on the Spectrin-Actin Junctions Leading to Erythrocyte Fragility and Hemolytic Anemia*

Received for publication, November 1, 2006 Published, JBC Papers in Press, December 2, 2006, DOI 10.1074/jbc.M610231200

Huiqing Chen[‡1], **Anwar A. Khan**[‡1], **Fei Liu**[§], **Diana M. Gilligan**[¶], **Luanne L. Peters**[‖], **Joanne Messick**[**], **Wanda M. Haschek-Hock**[**], **Xuerong Li**[‡], **Agnes E. Ostafin**[§], **and Athar H. Chishti**[‡2]

From the [‡]*Department of Pharmacology/Cancer Center, University of Illinois College of Medicine, Chicago, Illinois 60612, the* [§]*Department of Chemical Engineering, University of Notre Dame, Notre Dame, Indiana 46556,* [¶]*Puget Sound Blood Center, University of Washington School of Medicine, Seattle, Washington 98104,* [‖]*The Jackson Laboratory, Bar Harbor, Maine 04609, and the* [**]*Department of Comparative Pathology, University of Illinois, Urbana, Illinois 61802*

Dematin and adducin are actin-binding proteins of the erythrocyte "junctional complex." Individually, they exert modest effects on erythrocyte shape and membrane stability, and their homologues are expressed widely in non-erythroid cells. Here we report generation and characterization of double knock-out mice lacking β-adducin and the headpiece domain of dematin. The combined mutations result in altered erythrocyte morphology, increased membrane instability, and severe hemolysis. Peripheral blood analysis shows evidence of severe hemolytic anemia with reduced number of erythrocytes/hematocrit/hemoglobin and an ~12-fold increase in the number of circulating reticulocytes. The presence of a variety of misshapen and fragmented erythrocytes correlates with increased osmotic fragility and reduced *in vivo* life span. Despite the apparently normal protein composition of the mutant erythrocyte membrane, the retention of the spectrin-actin complex in the membrane under low ionic strength conditions is significantly reduced by the double mutation. Atomic force microscopy reveals an increase in grain size and a decrease in filament number of the mutant membrane cytoskeleton, although the volume parameter is similar to wild type erythrocytes. Aggregated, disassembled, and irregular features are visualized in the mutant membrane, consistent with the presence of large protein aggregates. Importantly, purified dematin binds to the stripped inside-out vesicles in a saturable manner, and dematin-membrane binding is abolished upon pretreatment of membrane vesicles with trypsin. Together, these results reveal an essential role of dematin and adducin in the maintenance of erythrocyte shape and membrane stability, and they suggest that the dematin-membrane interaction could link the junctional complex to the plasma membrane in erythroid cells.

The mechanical strength and stability of the erythrocyte membrane are regulated by a network of proteins that participate in both horizontal and vertical interactions. Spectrin, an abundant protein in the erythrocyte membrane cytoskeleton, plays a critical role in the maintenance of cell elasticity and membrane mechanical properties (1, 2). There is considerable interest in the elucidation of the mechanism by which elongated spectrin molecules are linked to the plasma membrane (1, 3–6). The spectrin heterodimer is believed to be anchored to the plasma membrane via two vertical attachment sites. The first attachment site is assembled by the band 3-ankyrin complex that binds to a site near the carboxyl terminus of β-spectrin, thus providing a mechanism by which the "head" region of the spectrin heterodimer binds to the cytoplasmic surface of the plasma membrane (1, 3, 4). The second vertical bridge is located at the "tail" region of the spectrin heterodimer and is composed of a complex of proteins collectively known as the "junctional complex" (5, 6). A prominent feature of the junctional complex is the presence of 37 nm actin protofilaments consisting of a precisely defined stoichiometry of ~13 actin monomers per oligomer (7). The current model of the red cell membrane predicts that protein 4.1, a major component of the junctional complex, participates in the regulation of both horizontal and vertical interactions of spectrin. Protein 4.1 binds to actin protofilaments and the amino terminus of β-spectrin thus stabilizing their horizontal interactions within the junctional complex. In addition, the amino-terminal FERM domain of protein 4.1 binds to the cytoplasmic domain of transmembrane glycophorin C, and this binding provides a mechanism for the vertical linkage of the junctional complex to the plasma membrane (1). This model of the red cell membrane has evolved based on *in vitro* protein binding studies and the biochemical characterization of erythrocyte membrane proteins from patients afflicted with various syndromes of inherited hemolytic anemia (1, 8, 9).

The actin-spectrin containing junctional complex serves as critical regulatory nodes for the maintenance of erythrocyte shape and membrane stability (1, 4, 6). The non-erythroid counterparts of the components of the junctional complex exist in many mammalian cells. Therefore, a precise understanding of the composition, organization, and the mode of membrane attachment of the various components of the junctional com-

* This work was supported by National Institutes of Health Grants HL051445 (to A. H. C.) and HL075714 (to L. L. P.). The costs of publication of this article were defrayed in part by the payment of page charges. This article must therefore be hereby marked "*advertisement*" in accordance with 18 U.S.C. Section 1734 solely to indicate this fact.

[1] Both authors contributed equally to this work.

[2] To whom correspondence and reprint requests should be addressed: Dept. of Pharmacology, UIC Cancer Center, 909 South Wolcott Ave., Rm. 5097, Chicago, IL 60612-3725. E-mail: chishti@uic.edu.

plex is of fundamental importance. Using immunogold electron microscopy, we have previously shown that dematin, adducin, and protein 4.1 are localized at the junctional complex (10). Several other proteins are also located at the junctional complex, including the tropomyosin, tropomodulin, p55, and calmodulin. The tropomyosin and tropomodulin appear to stabilize the length and stoichiometry of actin protofilaments and are likely to participate in the regulation of horizontal interactions between spectrin and actin protofilaments (11). The ternary complex between protein 4.1, p55, and glycophorin C is believed to provide a mechanism for the vertical linkage of the spectrin-actin junctions to the plasma membrane (5, 6, 12). *In vitro*, calmodulin regulates various interactions of the junctional complex in a calcium-dependent manner (13). In contrast, the function of dematin and adducin in the junctional complex remains poorly understood. Adducin and dematin are peripheral membrane proteins, and *in vitro* binding studies have shown that both can bind and bundle actin filaments (6, 14–19). In addition, adducin binds to calmodulin directly and promotes the assembly of spectrin and actin in a calcium- and calmodulin-dependent manner (16, 18, 20, 21). Both adducin and dematin are substrates of multiple protein kinases, and their phosphorylation status regulates interactions with spectrin and actin and with the plasma membrane (22). Despite a detailed knowledge of their domain organization and *in vitro* protein-protein interactions, the precise physiological function of adducin and dematin remains unclear in the mature erythrocyte plasma membrane.

Recently, two independent mouse models of β-adducin deficiency and one mouse model lacking the headpiece domain of dematin were generated (14, 23, 24). The impetus for the development of double knock-out mice lacking β-adducin and dematin headpiece came from the surprisingly mild phenotypes of erythrocyte shape and fragility observed in each of the three mouse models of β-adducin and dematin headpiece deficiency. Because of the fact that both dematin and adducin are located at the junctional complex and display similar actin binding properties, we speculated that they may perform a redundant function in the mature erythrocytes. To test this hypothesis, we generated the double knock-out mice lacking β-adducin and the headpiece domain of dematin. Hematological analysis of the double knock-out mice reveals a critical role of dematin and β-adducin in the maintenance of erythrocyte shape and membrane stability. Our results also demonstrate that dematin binds to red cell membrane inside-out vesicles in a saturable manner, and this binding is eliminated by the protease treatment of vesicles. Functional implications of these findings will be discussed.

MATERIALS AND METHODS

Generation and Identification of Double Knock-out Mice—Dematin (*Epb4.9*) and β-adducin (*Add2*) double knock-out (DAKO)[3] mice were generated by crossing of dematin (headpiece domain deletion) null (14) and β-adducin null (24) mice. The maps of the deletion constructs and targeting vectors have been described in the original publications (14, 24). The PCR strategy for genotyping the dematin KO mice has been described before (14). The PCR screen for β-adducin null genotype was performed with the following three primers in a single PCR: ADD-FA, TTT AGG CTG CCA TGG CTC AT; ADD-RB, GGT CAG GAC CTT ACA GTT CC; and ADD-NEO1, TCT ATC GCC TTC TTG ACG AG. The wild type allele produced a 380-bp fragment, and the KO allele resulted in the amplification of a 614-bp fragment. Adult mice of 3–6 months of age were used in the experiments reported here unless otherwise noted. All mice used were of C57BL/6J and 129/SVJ mixed genetic background.

Pathological and Hematological Analysis—Clinical pathology was performed by the Veterinary Diagnostic Laboratory of the University of Illinois, Urbana-Champaign. Peripheral blood, bone marrow, and spleen smears were stained with Wright-Giemsa. For hematological analysis, blood was collected in the heparinized syringes by cardiac puncture. Routine erythrocyte indices and reticulocytes were analyzed using a hemoanalyzer (Advia 120, Bayer Diagnostics) fitted with murine hematology software.

Scanning Electron Microscopy—Peripheral blood was collected in acid citrate dextrose, and the cells were washed and then fixed with 2% glutaraldehyde and 2% paraformaldehyde in 100 mM cacodylate buffer, pH 7.2, for 10 min (25). Erythrocytes were then allowed to attach to poly-L-lysine-coated coverslips for 1 h. Attached cells were dehydrated by immersion in ethanol gradient, dried in a critical point dryer, sputter-coated with gold, and viewed with JEOL 5600 LV scanning electron microscope (JEOL Ltd., Tokyo, Japan).

Preparation of Erythrocyte Ghosts, Triton Shells, and Inside-out Vesicles—Ghosts were prepared by hypotonic lysis of erythrocytes with 5.0 mM phosphate buffer, pH 7.4, containing 0.1 mM EDTA and 0.1 mM PMSF. With DAKO erythrocytes, some hemoglobin remains associated with the ghosts even after extensive washing steps. Triton shells or skeletons were prepared by incubation of erythrocyte ghosts with 1% Triton X-100 in 50 mM Tris-HCl, pH 7.5, 1.0 mM EDTA, 1.0 mM EGTA, 1.0 mM PMSF, and KCl either at 0.1 or 0.5 M concentration for 60 min at 4 °C. After centrifugation at 55,000 × *g* for 60 min at 4 °C, the skeleton pellets were rinsed gently with PBS to remove excess KCl and dissolved in the gel loading buffer at 37 °C for 30 min. IOVs were prepared by washing ghosts with 0.1 mM phosphate buffer, pH 8.0, 0.1 mM EDTA, 0.1 mM PMSF, 0.1 mM DTT and incubating washed ghosts in 3 volumes of the same buffer for 12 h on ice. IOVs were sedimented at 55,000 × *g* for 60 min at 4 °C and dissolved in the sample loading buffer for analysis.

SDS-PAGE and Western Blotting—Erythrocyte ghost proteins were separated on 8.5% polyacrylamide gels (26) and stained with Coomassie Blue. For immunoblotting, proteins were transferred to a nitrocellulose membrane (Bio-Rad), blocked with 5% milk in Tris-buffered saline containing 0.1% Tween 20, and incubated with the respective antibodies. Enhanced Chemiluminescence detection was carried out by using SuperSignal West Pico kit (Pierce).

[3] The abbreviations used are: DAKO, dematin-adducin double knockout; WT, wild type; DKO, dematin-headpiece knock-out; AKO, β-adducin knock-out; KO, knock-out; PBS, phosphate-buffered saline; AFM, atomic force microscopy; IOVs, inside-out-vesicles; NHS, *N*-hydroxysuccinimide; BSA, bovine serum albumin; DTT, dithiothreitol; PMSF, phenylmethylsulfonyl fluoride; RBC, red blood cells.

Antibodies—The antibodies used were as follows: dematin (affinity-purified polyclonal antibody against human erythrocyte dematin at 1:5000 dilution); β-adducin (polyclonal β-1 antibody at 1:2500 dilution); α-adducin (affinity-purified polyclonal antibody at 1:5000 dilution); p55 (mouse monoclonal antibody at 1:5000 dilution); ankyrin (polyclonal antibody at 1:5000 dilution); protein 4.2 (polyclonal antibody at 1:5000 dilution); glycophorin C (polyclonal antibody at 1:1000 dilution); glycophorin A (mouse monoclonal antibody at 1:1000 dilution); protein 4.1 (polyclonal antibody at 1:5000 dilution); band 3 (polyclonal antibody against cytoplasmic domain at 1:5000 dilution); spectrin (polyclonal affinity-purified against both α- and β-spectrin at 1:5000 dilution); and actin (monoclonal antibody from Sigma at 1:5000 dilution).

Determination of Erythrocyte Life Span—WT and DAKO mice were injected with *N*-hydroxysuccinimide (NHS)-biotin (25 μg/g body weight) through a tail vein injection. Five μl of blood was drawn in PBS-G (PBS supplemented with 10 mM glucose) every 5 days. Washed erythrocytes (2.0×10^7) were incubated with avidin/fluorescein isothiocyanate (20 μg in 500 μl of PBS-G) at 37 °C for 1 h. Erythrocytes were washed three times with PBS-G, and the percentage of labeled cells was determined by flow cytometry (FACSCalibur, BD Biosciences). The cell labeling was greater than 95%, and in most experiments, the labeling was close to 99%. The gate used for the WT samples was identical to that used for the DAKO samples. Therefore, very small vesicles and fragments were not counted as individual cells.

Osmotic Fragility Assay—Equal numbers of cells were mixed with NaCl solutions of varying osmolarities and incubated for 20 min at room temperature. After gentle centrifugation, the absorbance of the supernatant was determined at 540 nm. A_{540} of each sample in water was taken as 100% lysis, and readings of the same sample in various osmolarity solutions were normalized.

Cell Attachment and Cytoskeleton Exposure for Atomic Force Microscopy—Peripheral blood was collected from WT, DKO, AKO, and DAKO mice. Erythrocytes were washed with PBS and examined within 5 h. Cell attachment on glass coverslips was performed as described previously (27). Briefly, a suspension of washed erythrocytes was brought into contact with chemically modified glass coverslips coated with lectin, erythroagglutinating phytohemagglutinin, for 30 min to allow the cells to attach. The morphology of unattached and attached erythrocytes was examined by optical microscopy (Olympus X71). Erythrocytes attached to the lectin-coated coverslips were sheared open, and the cytoplasmic surface of the membrane was exposed by subjecting the attached cells to a stream of a partially hypotonic solution of 5P7-70 (5 mM KH_2PO_4/K_2HPO_4 and 70 mM NaCl, pH 7.4) at a rate of ~0.75 ml/s for 20 s through a 23-gauge needle. Slides were rinsed gently with 5P7-70 to remove loose fragments and cell contents. The specimens were fixed with 0.05% glutaraldehyde (freshly prepared in 5P7-70) for at least 30 min at 0 °C, to avoid damage from air drying (28), and then washed with fresh 5P7-70 to remove excess reagent. Slides were rinsed briefly with deionized water before air-drying in a covered Petri dish.

Atomic Force Microscopy—AFM topographic images of the exposed cytoplasmic surface of erythrocyte membranes were recorded with the Nanoscope III Multimode SPM™ system (Digital Instruments, CA) in the tapping mode. An E-scanning tube with a scan width of 15 μm was used. NanoSensors TappingMode™ Etched Silicon Probes OTESPA (Digital Instruments, CA) with a tip radius of 5–10 nm, a spring constant k = 20–100 newtons/m, and a resonant frequency f_0 = 200–400 kHz were used for tapping mode imaging. Briefly, the sensitivity and linearity of the scanner were calibrated with a NanoGauge™ NGR-1 calibration reference (NanoDevices, Santa Barbara, CA). *X-Y* calibration was performed using capture calibration. Fine-tuning was performed to correct both *X-Y* and *Z* measuring accuracy. The *z*-piezo sensitivity was calibrated to be ~7.56 nm/V, and the effective system *z*-resolution was ~6.71 mV/LSB, which is about 440 V spanning a total of 65,536 relative height bins. For AFM imaging, the coverslips with attached membrane material were glued to 1.0-mm thick steel plates with a diameter of 15 mm using the double-sided adhesive tape and mounted on the magnetic AFM scanning stage. The AFM measurements were performed at an ambient air pressure and room temperature. In the tapping mode, the resonant frequency of the cantilever was selected automatically by the system with the typical values around ~300 kHz. Images for analysis were obtained at a scan rate of about 1–2 Hz for scan sizes ranging from 15 to 0.5 μm with a resolution of 512 × 512 pixels and an image depth of 16-bit.

Image Analysis—Image processing and analysis were performed using Nanoscope III 5.12r3 software (Digital Instruments, CA). Height profiling, histogram construction, bearing analysis, and grain size analysis were performed as described previously (28). Histograms were fitted with gaussian peaks in Origin Pro 7.0 software (Northampton, MA) to calculate peak positions, which were used to determine thresholdings in bearing and grain size analysis. The volume of the imaged specimen was calculated as described previously (28). Analysis of the cytoskeleton was performed using Fovea Pro version 3 software (Reindeer Graphics, NC) to generate the cytoskeleton connectivity map.

Actin Staining—RBCs were collected in PBS-GB (PBS supplemented with 10 mM glucose and 0.1% BSA). After washing with PBS-GB, cells were allowed to attach to poly-L-lysine-coated coverslips for 1 h. Cells were then lysed by treatment with 0.0075% saponin for 2 min. Ghosts were fixed with 0.5% glutaraldehyde for 20 min, labeled with 0.01% phalloidin-Alexa-595 (Molecular Probes) for 1 h, and viewed with Zeiss LSM 510 inverted confocal microscope.

Dematin Binding to Stripped IOVs—Dematin was isolated from human erythrocyte ghosts as described before (29). Purified dematin recovered from the Mono Q column (FPLC) was dialyzed against the column buffer (20 mM Tris-HCl, pH 8.3, 1.0 mM EGTA, 0.5 mM DTT, 0.02% NaN_3) and examined for its actin binding and bundling activity before using in the membrane binding assays. Alkali-stripped membrane vesicles were prepared using a protocol established previously (30). Briefly, human erythrocyte ghosts were sequentially stripped of the glycolytic enzymes, spectrin-actin, and other peripheral membrane proteins using solutions of low ionic strength, high salt, and at pH 12, respectively (30). The stripped IOVs were washed with 5.0 mM sodium phosphate, pH 8.0, 1.0 mM EDTA, supplemented with 10 mg/ml of sucrose, and frozen in the liquid

nitrogen. The alkali-stripped IOVs were free of endogenous dematin as confirmed by Western blot analysis.

Binding assays were performed in a total volume of 50 μl where increasing concentrations of dematin were incubated with a constant amount of stripped IOVs in 100 mM KCl, 2.0 mM $MgCl_2$, 5.0 mM sodium phosphate, pH 7.6, 1.0 mM DTT, and 1.0 mg/ml BSA. Alternatively, the alkali-stripped IOVs were digested with trypsin (1.0 μg/ml) on ice, and the protease activity was quenched as described before (30). After incubation with purified dematin for 90 min at room temperature, vesicles were centrifuged at 20,000 rpm for 25 min (type 42.2 Ti Beckman rotor), and pellets were dissolved in 100 μl of sample buffer containing 0.5% SDS. A portion of the solubilized pellet was diluted in the Triton-containing buffer to reduce the concentration of SDS to 0.0075%. Quantification of dematin was carried out by an enzyme-linked immunoassay as described before (31). Protein concentrations of purified dematin and stripped IOVs were determined by the Bradford assay (32) and SDS-PAGE using BSA as a standard.

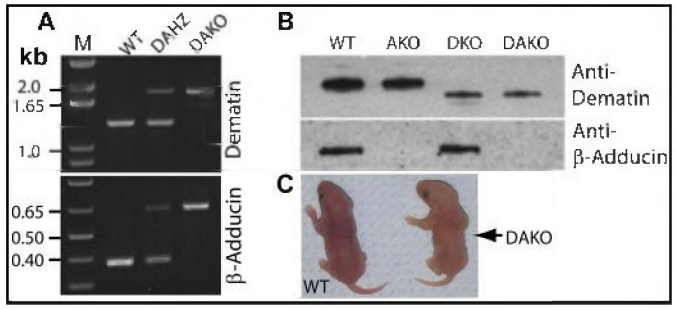

FIGURE 1. **PCR and Western blot analysis of DAKO mice genotype and a comparison of 1-day-old WT and DAKO pups.** *A*, PCR on DNA from WT mice results in a single product for both dematin and β-adducin genes (*lane WT*), the heterozygous genotype for both genes produces two products of expected sizes (*lane DAHZ*), and the DAKO genotype produces only the larger sized product (*lane DAKO*). *Lane M* shows size markers. *B*, Western blots demonstrate the presence of both proteins in the WT erythrocyte ghosts (*lane WT*), the complete absence of β-adducin in AKO ghosts (*lane AKO*), a truncated (headpiece domain deletion) dematin in DKO ghosts (*lane DKO*), and the absence of β-adducin with truncated dematin in DAKO ghosts (*lane DAKO*). *C*, comparison of WT and DAKO pups at day 1 of birth. Note relative pallor of DAKO pup as compared with WT pup.

RESULTS

Dematin and Adducin Double Knock-out (DAKO) Mice Are Viable—Single knock-outs of dematin headpiece and β-adducin mice have been described before (14, 23, 24). For simplicity, we will refer to these mouse models as dematin knock-out (DKO) and adducin knock-out (AKO) in the rest of this paper. DAKO mice were generated by crossing the heterozygous DKO and AKO mice, and their genotype was confirmed by PCR and Western blot analysis (Fig. 1). The dematin genotyping strategy produces a 1.3-kb band with the WT genotype, a 1.7-kb band with the KO genotype, and both bands with the heterozygous genotype (Fig. 1*A*, *lanes WT, DAKO,* and *DAHZ*). Similarly, the PCR strategy for β-adducin produces a 380-bp band with the WT genotype, a 614-bp band with the KO genotype, and both bands with the heterozygous genotype (Fig. 1*A*, *lanes WT, DAKO,* and *DAHZ*). A polyclonal antibody against human erythrocyte dematin recognizes a 48-kDa polypeptide in WT genotype erythrocyte ghosts and a truncated protein (~40 kDa) in DKO and DAKO genotypes (Fig. 1*B*, *lanes DKO* and *DAKO*). The 52-kDa subunit of dematin is also detectable in WT ghosts at higher protein concentrations. It is noteworthy that although the truncated 40-kDa dematin polypeptide is synthesized in the KO erythrocytes, its stable incorporation into the mutant erythrocyte ghosts is reduced by ~70%. Similarly, a polyclonal antibody against β-adducin recognizes an ~102-kDa protein in WT erythrocyte ghosts but did not recognize a protein band in the ghosts from AKO or DAKO genotypes (Fig. 1*B*, *lanes AKO* and *DAKO*). It was shown previously that the amount of α-adducin was reduced by ~75% in the β-adducin null mice, whereas γ-adducin was up-regulated ~500% (23, 24). Together, these results demonstrate successful generation of DAKO mice. These mice are distinguishable at birth by their pallor as compared with the other genotypes. The overall phenotype of WT and DAKO mice at day 1.0 after birth is shown in Fig. 1*C*. DAKO mice are indistinguishable from WT animals at 10 days after birth. No striking physical abnormalities are detected in the DAKO mice apart from the frequent loss of hair around the nose and face in most mature adults.

DAKO Mice Show Severe Hemolytic Anemia—Anatomic pathology findings did not differ between WT and single KO mice. The DAKO mice show evidence of a hemolytic but regenerative anemia related to severe hemolysis. The regenerative erythropoiesis is primarily evident in the spleen, but it is also detectable in the liver and is erythroid in nature. *In vivo* hemolysis results in excessive circulating iron, which is taken up by the Kupffer cells and to a lesser extent by hepatocytes, renal proximal tubular epithelial cells, and reticulo-endothelial cells in the spleen. Normal splenic extramedullary hematopoiesis is observed in WT spleen with both the myeloid and erythroid series cells present. By contrast, splenic tissue from DAKO mice shows extensive extramedullary hematopoiesis, which is comprised predominantly of erythroid cells (erythroid hyperplasia). There are multiple foci of extramedullary erythropoiesis in the liver of DAKO mice, as well as brown pigment in the Kupffer cells, and to a lesser extent in the hepatocytes. In contrast, the liver tissue of WT and single KO mice do not show any foci of erythropoiesis or pigment accumulation.

The hematological indices of DAKO mice are markedly different from those of WT or single KO animals. A significant decrease is observed in the erythrocyte count ($5.3 \times 10^6/\mu l$), hemoglobin (7.1 g/dl), and hematocrit (21.7%) (Table 1). The high reticulocyte count (~46%, ~12-fold increase) in the peripheral blood of adult DAKO mice indicates a regenerative anemia and explains the severe splenomegaly observed upon pathological examination. At birth, the peripheral blood from DAKO pups had ~20% reticulocytes, and this increased to ~30% by the age of 10 days and reached ~46% in adulthood. The serum total bilirubin level of DAKO mice also increased to 3–6 times the normal values. In the kidneys of DAKO mice, the proximal tubular epithelial cells contained large amounts of brown pigment that stained with Prussian blue, consistent with chronic intravascular hemolysis. In addition, there is evidence of mild scattered tubular epithelial cell apoptosis. These changes are not present in the kidneys of WT or single KO mice. Pathological examination of other organs, including the heart, skeletal muscle, lung, trachea, esophagus, thymus, thy-

roid, parathyroid, adrenal, pancreas, gastrointestinal tract, lymph node, urogenital tract, brain, salivary gland, and spinal cord, did not reveal any significant differences between WT, single KO, and DAKO mice.

DAKO Erythrocytes Display Considerable Variation in Shape and Size—The peripheral blood of DKO mice contains spherocytes (14), whereas AKO mice show the presence of spherocytes, spherostomatocytes, and rounded elliptocytes (23, 24). In contrast, the DAKO mice exhibit marked anisocytosis with moderate schistocytes and spherocytes and polychromasia (Fig. 2). In addition, the presence of fragmented erythrocytes, ghosts, acanthocytes, and the high number of spherocytic microcytes indicates a severe hemolytic process. The pathophysiology behind the development of these spherocytes may involve both an erythrocyte membrane defect and the selective sequestration of cells within the spleen. The erythrocyte distribution histogram is wide, and the red cell distribution width is high, indicating a tremendous variation in cell size (data not shown). The occurrence of microcytic (spherocytic microcytes) as well as macrocytic erythrocytes (polychromatophilic cells-putative reticulocytes) results in a mean corpuscular volume that falls within the normal range (Table 1). It is noteworthy that despite the high reticulocytosis, we do not observe any nucleated erythroid cells in the peripheral blood. Erythrocyte morphology was also analyzed by scanning electron microscopy. DAKO erythrocytes show marked anisocytosis and include schistocytes (Fig. 3). Microcytic vesicles are seen budding off the erythrocytes (Fig. 3, *filled arrows*), and short, elongated, or coiled protruding filamentous structures are also observed (*arrows*). Both the microcytic vesiculation and the protruding structures are also observed in band 3 knock-out erythrocytes (33, 34). Neither the filamentous structures nor the microcytic vesiculation is observed in single KO or WT mice.

TABLE 1

Hematological indices of WT, AKO, DKO, and DAKO mice

The mean represents averages derived from six WT, three AKO, three DKO, and five DAKO mice, respectively. DAKO mice have severe anemia with marked reticulocytosis. Despite the presence of these macrocytes, the mean corpuscular volume is within the normal range indicating the presence of an equivalent population of microcytes. RBC, red blood cells ($10^6/\mu l$); HGB, hemoglobin (g/dl); HCT, hematocrit (%); MCV, mean corpuscular volume (fl); MCH, mean corpuscular hemoglobin (pg); MCHC, mean corpuscular hemoglobin concentration (g/dl); Retic, reticulocytes (%). *, $p < 0.05$; ***, $p < 0.001$.

	WT	AKO	DKO	DAKO
RBC	8.5 ± 0.8	10.4 ± 0.5*	8.2 ± 1.2	5.3 ± 0.7***
HGB	13.6 ± 0.7	15.2 ± 0.9	11.9 ± 1.5	7.1 ± 0.6***
HCT	41.1 ± 3.6	44.3 ± 3.4	34.4 ± 5.6	22.8 ± 2.6***
MCV	48.4 ± 2.5	42.8 ± 1.1	41.8 ± 1.0	47.9 ± 7.1
MCH	16.1 ± 0.8	14.7 ± 0.1	14.6 ± 0.4	15.1 ± 3.2
MCHC	33.3 ± 1.7	34.0 ± 0.3	34.9 ± 1.3	31.2 ± 2.3
Retic	3.8 ± 2.1	5.6 ± 2.0	4.3 ± 2.4	45.9 ± 7.0***

In WT and single KO spleens, most of the erythroid precursors are orthochromatic normoblasts (data not shown). The spleens from both single KO genotypes show a relative increase in the number of macrophages containing pigmented material consistent with hemosiderin. Orthochromatic normoblasts consist of the most common cell type observed in the spleen of DAKO mice, and erythroid precursor cells, including erythroblasts, are also seen. The bone marrow cellularity of all four genotypes is similar (~90%). Bone marrow from WT and single KO mice shows synchronous maturation of all cell lineages, whereas bone marrow from DAKO mice shows erythroid hyperplasia, with ~50% reduction in the myeloid to erythroid ratio (data not shown). The erythroid lineage matures normally, but a mild increase of mitotic figures in precursor cells is also observed. Cellular maturation of the myeloid and megakaryocytic lineages is synchronous, and the number of megakaryocytes is normal to slightly increased.

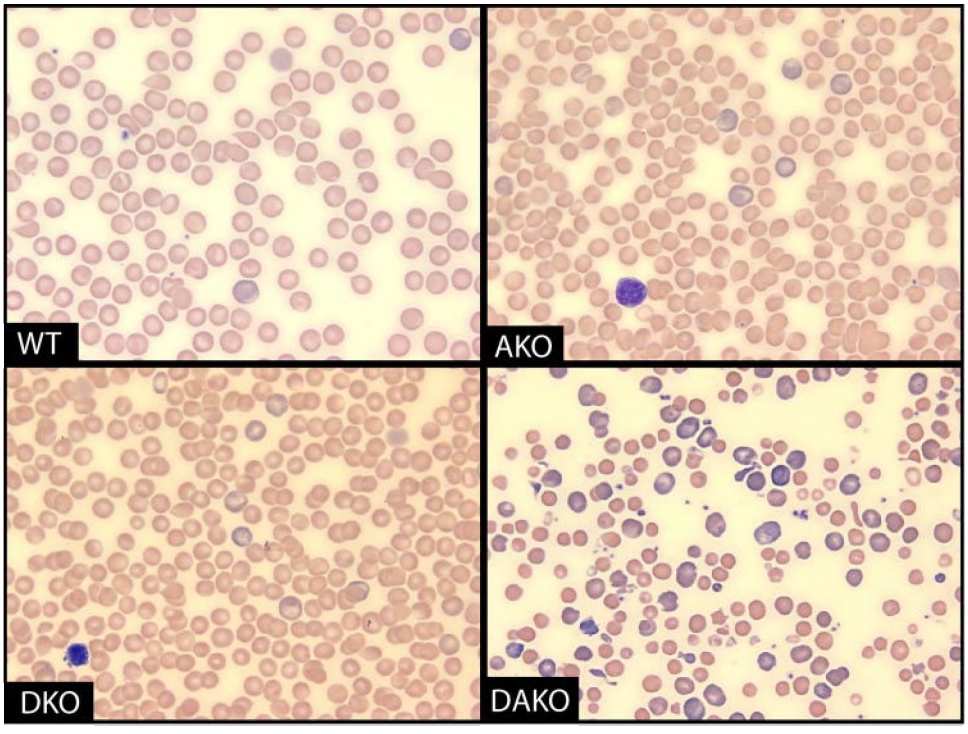

FIGURE 2. **Comparison of peripheral blood smears obtained from WT, AKO, DKO, and DAKO adult mice (Wright-Giemsa stain).** The peripheral blood smear from DKO mice contains spherocytes, although blood from AKO mice also demonstrates spherocytes and rounded elliptocytes. In contrast, the smear from DAKO mice exhibits marked anisocytosis with moderate schistocytes and spherocytes, indicating a severe hemolytic process (×100 magnification).

DAKO Mice Have Fragile Erythrocytes with a Shortened Half-life—Osmotic fragility measurements reveal an intermediate fragility of DAKO erythrocytes as compared with single KOs. The 50% hemolysis is achieved at 195, 215, 250, and 242 mosM salt for WT, DKO, AKO, and DAKO erythrocytes, respectively (Fig. 4*A*). The DAKO erythrocytes are clearly more fragile than both single knock-out mice, exhibiting intravascular hemolysis *in vivo*, as evident by the presence of significant free hemoglobin in the plasma (Fig. 4*C*). The first part of the fragility curve (260–300 mosM) shows

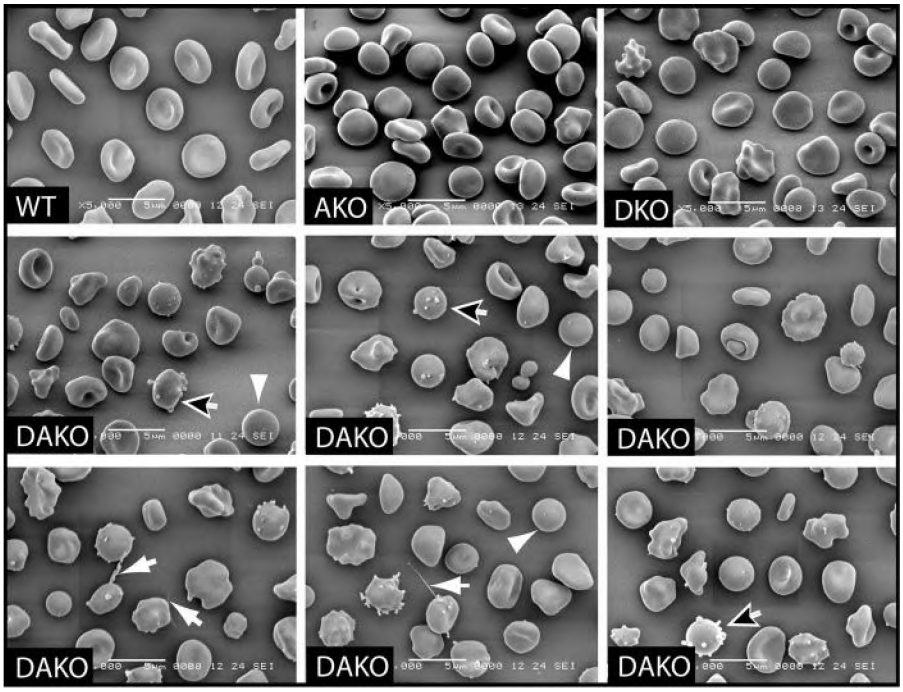

FIGURE 3. **Scanning electron microscopy of WT, AKO, DKO, and DAKO peripheral blood cells.** DAKO RBCs show considerable variation in shape and size. *Bar* represents 5 μm. *Arrows*, filamentous membrane extensions; *arrowheads*, spherocytes; *filled arrows*, cells losing microcytic vesicles.

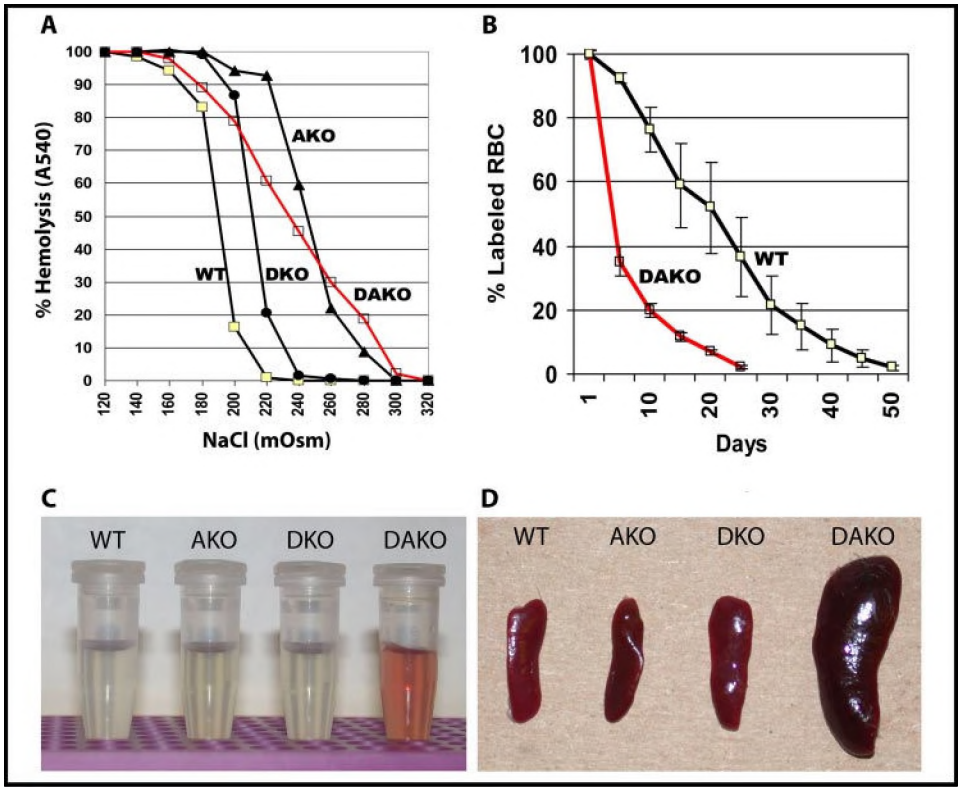

FIGURE 4. **Evaluation of hematological parameters.** *A*, osmotic fragility of WT, AKO, DKO, and DAKO erythrocytes. Tests were performed as described under "Materials and Methods," and the averages of five readings are shown. *B*, *in vivo* analysis of mouse erythrocyte life span. Five WT and 6 DAKO mice were injected with NHS-biotin and analyzed for erythrocyte labeling at constant intervals as described under "Materials and Methods." The rapid loss of label from DAKO mice blood is because of increased erythrocyte turnover. The initial level of labeling (95–100%) was used to normalize subsequent readings. *C*, hemolysis of DAKO mutant erythrocytes. Equal volumes of anticoagulated fresh blood and PBS were mixed and centrifuged gently to remove intact cells. The supernatant containing the PBS diluted plasma from WT, AKO, DKO, and DAKO mice was collected and photographed. *D*, splenomegaly in mutant mice. DAKO mice demonstrate marked splenomegaly.

the highest fragility for DAKO erythrocytes. In this region, mature and more fragile erythrocytes are likely being lysed. The remaining DAKO erythrocytes show more resistance to lysis in the 160–200 mosM range as compared with single KO erythrocytes. It is noteworthy that the intermediate fragility of DAKO erythrocytes is likely to originate from the increased number of reticulocytes (>45%). The presence of a mixture of reticulocytes, microcytes, and macrocytes in the region of 160–200 mosM range presumably contributes to the development of a shallow slope in the fragility curve of DAKO erythrocytes. Despite repeated attempts, it was not feasible to separate mature erythrocytes from reticulocytes in the DAKO mice, a situation akin to the development of high reticulocytosis in the band 3 null mice (33, 34).

The red cell half-life was determined by *in vivo* NHS-biotin labeling of erythrocytes. Red cell half-life was reduced from 22 days in WT mice to less than 5 days in DAKO mice (Fig. 4*B*). Our prediction is that the steeper slope accounts for the clearance of mature erythrocyte population, whereas the shallow slope presumably originates from the circulating labeled reticulocytes that behave more like sturdy normal erythrocytes. Because of extensive heterogeneity of the cell population in DAKO samples, it remains a possibility that only a fraction of reticulocytes mature normally when released in the peripheral circulation. Overall, our results indicate rapid clearance of mutant erythrocytes in DAKO mice, and a need for increased erythropoiesis, which results in marked splenomegaly (Fig. 4*D*). The average spleen weight of DAKO mice was ~2–4% of body weight as compared with 0.3% for WT mice.

Retention of the Spectrin-Actin Complex Is Altered in DAKO Erythrocytes—To investigate the mechanism of erythrocyte membrane fragility, a survey of protein profiles in erythrocyte ghosts, IOVs, and skeletons was performed (Fig.

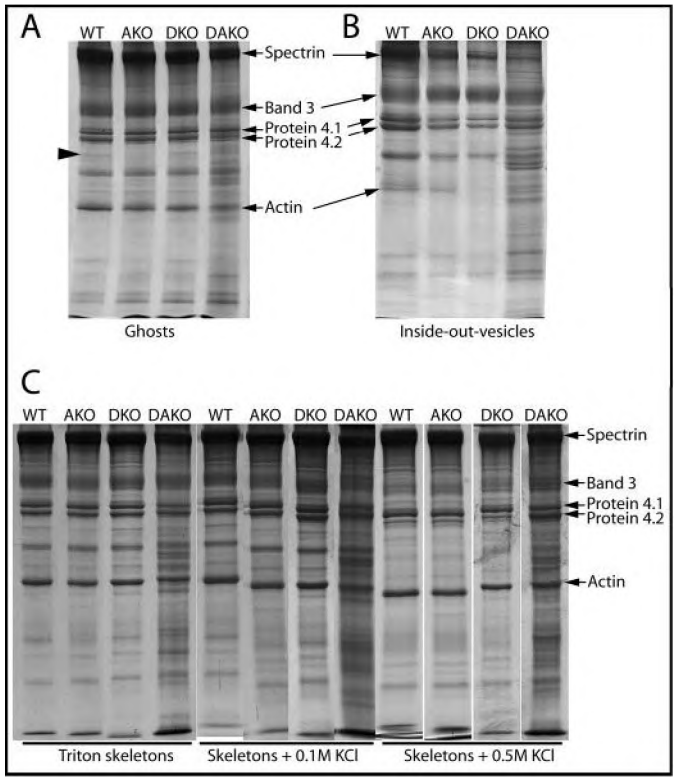

FIGURE 5. **Analysis of erythrocyte membrane proteins.** *A*, ghosts (*A*), inside-out vesicles (*B*), and Triton shells of WT, AKO, DKO, and DAKO erythrocytes (*C*) were prepared as described under "Materials and Methods." Proteins were separated by SDS-PAGE and stained with Coomassie Blue. Band 3 was used to normalize equal amounts of total protein in various lanes. The *arrowhead* in *A* indicates the position of ~65-kDa protein missing in the AKO ghosts. Gels were purposely overloaded to visualize the differential expression of minor proteins as shown in *A*. Lower protein loading gels of individual knock-out mice have been published before. It is noteworthy that the separation of mature erythrocytes from reticulocytes was not feasible in the DAKO mice presumably because of the extreme fragility of mature erythrocytes.

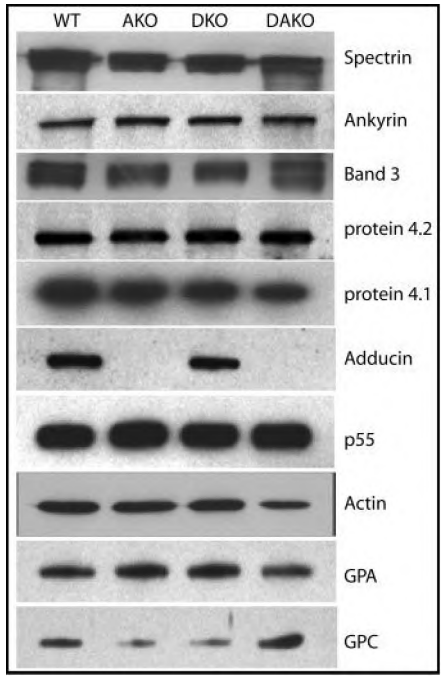

FIGURE 6. **Western blot analysis of selected proteins in WT, AKO, DKO, and DAKO erythrocyte ghosts.** Protein amounts were normalized based on Coomassie staining of band 3. Blots were probed with various antibodies, and bands were detected using the secondary antibody conjugated to horseradish peroxidase.

5). DAKO ghosts retain relatively more hemoglobin as compared with single KO ghosts, and the extensive reticulocytosis also contributes to the complexity of the protein profile in DAKO samples. For ghosts, IOVs, and Triton shells (without KCl), proteins were normalized by equal staining of band 3 protein in the Coomassie Blue gels. In one AKO report, no differences were observed in the protein compositions of WT and AKO ghosts (24). However, another AKO study reported the absence of a 65-kDa band both in ghosts and skeleton preparations, a slight reduction (~15%) in actin levels in the skeleton fraction, and an increase in the amount of various polypeptides of less than 40 kDa in ghosts and skeletons (23). Our analysis of AKO erythrocytes indicates a significant reduction of the ~65-kDa protein in ghosts and skeletons fractions (Fig. 5, *A* and *C, lane AKO*). Previously, the DKO skeletons and IOVs were shown to retain reduced amounts of actin and spectrin (14). The α-spectrin to band 3 ratio was reduced by ~60% in the DKO null IOVs (14). In DAKO ghosts, spectrin and actin are slightly reduced as compared with the WT erythrocytes (Fig. 5*A, lane DAKO*). Densitometric analysis of Western blots indicates ~15% reduction of both spectrin and actin in the DAKO ghosts as compared with the WT ghosts. In addition, several polypeptides in the range of 20–90 kDa are over-represented in the DAKO ghosts presumably because of high reticulocytosis.

In addition, the DAKO skeletons show a modest decrease in the retention of protein 4.1, as well as reduced amounts of actin and spectrin (Fig. 5*C, 1st panel, lane DAKO*). The elution of spectrin from the IOVs of DAKO cells is significantly greater as compared with WT or single knock-outs (Fig. 5*B, lane DAKO*). Densitometric analysis of Western blots revealed that spectrin is reduced by ~75% in the DAKO IOVs. Quantification of actin is difficult in the DAKO IOVs because of virtually complete removal of actin. However, visual inspection of the Coomassie Blue-stained gels suggests that actin is significantly reduced in the DKO IOVs as compared with WT mice (Fig. 5*B, lane DKO*), implying that at least a similar or greater elution of actin would take place from DAKO IOVs. Together, our results suggest a greater propensity of spectrin and actin dissociation from the DAKO erythrocyte ghosts when they are subject to low ionic strength extraction conditions. There are no significant alterations in the amounts of glycophorin A, ankyrin, protein 4.2, and p55 either in single KOs or DAKO erythrocytes (Fig. 6). The amount of glycophorin C appears to be slightly reduced in the DKO and AKO ghosts, whereas the level of protein 4.1 is slightly reduced in the DAKO ghosts. Previous studies have shown that α-adducin is reduced by ~80% in the β-adducin null erythrocytes (24). In our Western blots, we were unable to detect any α-adducin in the AKO or DAKO erythrocyte ghosts presumably because of the low reactivity of the polyclonal antibody directed against α-adducin. It is noteworthy that a precise quantification of the loss or gain of various polypeptides is not feasible here because of extensive reticulocytosis in the DAKO mice. Our repeated attempts failed to separate mature erythrocytes from reticulocytes in the DAKO blood, presumably because of the extreme fragility of mature erythrocytes. A similar limitation has

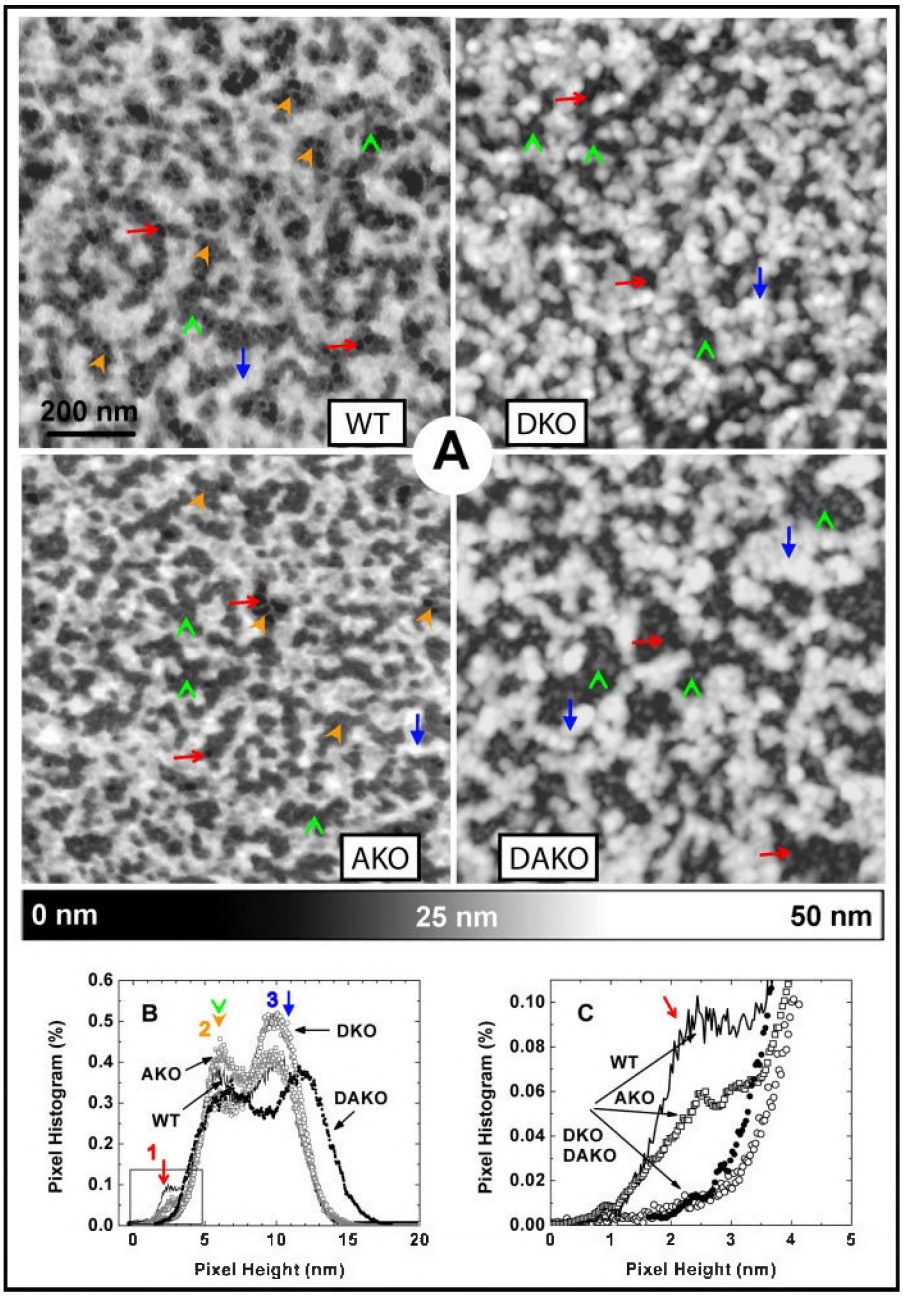

FIGURE 7. **AFM images of mouse erythrocyte cytoskeleton.** *A*, WT erythrocyte cytoskeleton with fine filaments features. DKO cytoskeleton with more aggregation and no fine filament features. AKO cytoskeleton with similar morphology as WT but more coarse features and less fine details. DAKO cytoskeleton with much more aggregation and network damage. *B*, WT and AKO samples have similar peak distributions; however, the WT histogram reveals more structural details as indicated by the extra small peak at lower pixel height. The DKO specimen histogram demonstrates a larger peak at higher pixel height, suggesting increased aggregation of the cytoskeleton filaments, although the apparent cytoskeleton height (distance between the two major peaks in histogram) is not significantly changed. As expected, the apparent cytoskeleton height in the DAKO specimen histogram is much larger than that of WT, indicating an increase in filaments aggregation. *C*, detailed view of the *left-most peak* region of *B* showing the alignment of the lipid bilayer peaks. *Red arrows*, top of lipid bilayer; *blue arrows*, coarse, tallest features; *gold arrowheads*, fine structure mesh; *green arrowheads*, intermediate height aggregates.

DAKO Erythrocyte Cytoskeleton Is Damaged and Aggregated—AFM, with its nanometer resolution, is capable of observing intact cellular architecture in three dimensions. AFM has been used previously to investigate erythrocyte cytoskeleton architecture and its stability without removing the plasma membrane by detergent treatment and without extending or staining the cytoskeleton (27, 28). This method, which provides information on native skeleton structure, reveals differences in the skeletal structures between WT, single KO, and DAKO erythrocytes. Low magnification AFM images (not shown) of glutaraldehyde-fixed WT and single KO skeletons show similar characteristics, whereas a large number of DAKO erythrocytes appeared damaged once sheared opened on the coverslip surface. At higher magnification (Fig. 7*A*), the AFM topography of WT mouse erythrocytes reveals individual thin filaments ~20–40 nm in length and ~7 nm in diameter (*gold arrowheads*), with similar dimensions of filaments in the intact cytoskeleton as reported previously in EM study (35). However, larger coarse features dominate the whole topography (Fig. 7*A*, *blue arrows*) suggesting filament aggregations, although fine filaments are observed in "window regions" framed by coarse mesh. For AKO specimens, the coarse mesh has smaller windows that obscure the fine filament details. For DKO and DAKO specimens, the "window" regions of the coarse mesh are filled with aggregated structures of intermediate height, and relatively few deep holes are observed.

For general estimation of the surface topology and sample orientation, a section profile at a specific position of the AFM topographic image along a selected direction is commonly used to directly measure the height of the surface feature. However, for more quantitative analysis of complex features such as in Fig. 7, a consistent and statistical method is required. The pixel histogram provides such a statistical means for comparing surface topography with similar features. The pixel histogram is defined as follows: pixel histogram (%) = $H_f(z)/H_f \times 100\% \approx$

been encountered before in the band 3 null mice that also show extensive reticulocytosis and highly fragile erythrocytes (33, 34). All measurements on band 3 null mice published to date have been made on a mixture of mature erythrocytes and reticulocytes (33, 34). Here the main intent of our studies was to identify any major loss of erythrocyte polypeptides in DAKO mice by using a combination of gel electrophoresis and Western blotting techniques.

TABLE 2
Characteristic AFM parameters of mutant cytoskeleton

Sample	WT	AKO	DKO	DAKO
D(2-1)	3.5 ± 1.2*	3.7 ± 1.4*	3.8 ± 1.5*	4.8 ± 1.8*
D(3-1)	7.4 ± 1.8*	7.1 ± 2.0*	7.9 ± 2.4*	10.5 ± 2.7#
Volume (10^6 nm^4)	4.78 ± 0.43*	4.13 ± 0.57*	5.07 ± 0.72*	4.53 ± 0.67*
Grain size (10^3 nm^2)	0.26 ± 0.18*	0.32 ± 0.18*	0.44 ± 0.27*	0.93 ± 0.39#
Filament no. (per μm^2)	807 ± 93*	674 ± 50*	109 ± 25#	74 ± 20#

* Indicates no significant difference between the data sets according to one-way analysis of variance test at 0.05 significant level ($p > 0.4$); # indicates significant difference of data set from the others ($p < 0.01$).

probability density of the pixel height, where $H_f(z)$ is the number of pixels in the topographic image with a height of z nm, and H_f is the total number of pixels in the topographic image. As suggested by the definition, pixel histogram gives an indication of the height distribution over the surface as well as the statistical deviation of the height from an average value. Instead of measuring the height at an individual position, all the pixels in a topographic image are counted to reflect the vertical trend of the measured surface features.

The pixel height histogram derived from the AFM images of WT mouse erythrocyte cytoskeleton corresponds to a multilevel network structure. Because all of the images shown in Fig. 7 are from lower magnification images (15 μm) where the lectin-coated coverslip surface was imaged, it is possible to calibrate the image height relative to this "zero" level in the histogram. The histogram from the WT specimen exhibits three major peaks (Fig. 7*B*), which corresponds to the cytoplasmic surface of the plasma membrane, intermediate height proteins in or just above the membrane, and larger protein aggregates. More discussion on this assignment is presented below. The lowest height peak 1 (Fig. 7*C*, is an expanded view of the *leftmost region* in Fig. 7*B*) corresponds to the top of the lipid bilayer (typical regions indicated by *red arrows* in Fig. 7*A*), whereas the rightmost peak 3 represents the coarse, tallest features in the image (typical regions indicated by *blue arrows* in Fig. 7*A*) that appears to be covered with the fine structure mesh. The middle peak 2 of the pixel height histogram reflects parts of the fine structure mesh (typical regions indicated by *gold arrowheads* in Fig. 7*A*) collapsed onto the surface of the lipid bilayer beneath, as well as intermediate height aggregates (typical regions indicated by *green arrowheads* in Fig. 7*A*) found within windows of the coarse network. The relatively small pixel height value for peak 1 reflects the lower position of the imaged lipid bilayer surface in the topographic image, whereas its small histogram value (%) indicates only a small amount of such regions with low height was imaged. On the other hand, the relatively large value of pixel height and histogram in peaks 2 and 3 suggests that features with larger height predominantly occupied the sample surface.

Peak separations between the centers of the middle peak and leftmost peak, D(2-1), and the centers of the right-most peak and leftmost peak, D(3-1), represent the average elevation of the fine filament features and the coarse aggregates from the bilayer surface, respectively. These values are listed in Table 2, along with other characteristic parameters typically considered in AFM image analysis of the cytoskeleton specimens (24). No significant difference for D(2-1) or D(3-1) exists among WT, AKO, and DKO specimens ($p > 0.4$, one-way analysis of variance). However, the corresponding values for the DAKO specimens are significantly different from the others ($p < 0.01$, one-way analysis of variance). In this case, the total height spanned between the highest and lowest features of the image is much greater and, given the large mesh size of the coarse features, suggests that significantly more aggregation of the cytoskeletal components occurs in DAKO mice erythrocytes. This conclusion can also be drawn based on the fact that the total volume of the cytoskeleton imaged in the WT, AKO, DKO, and DAKO erythrocytes was roughly equivalent over identical image areas. A constant cytoskeleton object image volume over a given image area suggests that the change in the cytoskeleton height is primarily because of a redistribution of the cytoskeletal proteins over the membrane plane, rather than due to differences in binding of the specimen to the coverslip, such as stretching or compression. The volume analysis of the cytoskeletal components in these images deviated between samples more than for human erythrocytes. This could be due to differences in the carbohydrate distribution of the murine erythrocytes or their interactions with the lectin coating below, especially for the mutants. Another explanation could be that the murine erythrocytes were not separated on the basis of cell age, and it is not clear whether the cell age influences the network density of the cytoskeleton in the mouse.

The fine filament structure seen in the WT mice is somewhat obscured in the AKO cytoskeleton, and the grain size of the coarse features is increased slightly. In the case of DKO, because the association with the plasma membrane is presumably compromised, this allows the spread of the coarser, taller features over the membrane. In the case of DAKO mice, both assembly reinforcements are eliminated resulting in very large windows in the coarse taller mesh. This latter feature exposes a large expanse of disassembled fine filament structure, possibly still tethered to junctional complex embedded in the phospholipid bilayer. An alternative possibility is that the remaining core domain of dematin that is incorporated into the membrane of DAKO erythrocytes at reduced amounts could be mediating the residual attachment of the junctional complex in DAKO erythrocytes.

AFM findings were further corroborated by the actin staining of WT and DAKO ghosts with phalloidin, which revealed a punctate and dense pattern in DAKO ghosts (Fig. 8). These results suggest aggregation of the skeleton in DAKO RBC ghosts as observed in AFM images. A greater number of RBC ghosts from DAKO peripheral blood were stained to higher extent as compared with ghosts from the WT mice.

Interaction of Dematin with the Erythrocyte Plasma Membrane—Evidence suggests that dematin may bind to a protein(s) associated with the erythrocyte plasma membrane. When human erythrocyte ghosts are incubated in the low ionic strength solution at 37 °C, more than 90% of the total spectrin

and actin is extracted in the supernatant. The pellet, which is predominantly composed of IOVs, retains ~70% of endogenous dematin (36). This observation suggests that dematin is bound to IOVs by a mechanism that is independent of its binding to the spectrin-actin complex. To test this possibility, we measured binding of purified native dematin to the alkali-stripped IOVs that are completely deficient of endogenous dematin and nearly all other peripheral membrane proteins (Fig. 9*A*). Human erythrocyte dematin bound to the stripped IOVs in a saturable manner (Fig. 9*B*), and the dematin-membrane binding was reduced substantially (~80%) upon pretreatment of stripped IOVs with trypsin (Fig. 9*B*). We used two negative controls to validate the specificity of dematin binding to the IOVs. In the first control, the stripped IOVs were analyzed without any exogenous dematin (Fig. 9*B*), and in the second negative control, dematin was incubated with liposomes composed of phosphatidylserine, phosphatidylethanolamine, and cholesterol. In both cases, no significant binding of dematin was detectable under the same binding conditions that were used for measuring the association of dematin with IOVs (data not shown).

It is noteworthy here that the alkaline treatment of human erythrocyte IOVs results in the denaturation of the cytoplasmic domain of band 3 but leaves its transmembrane domain in native form (37). In contrast, the extraction of IOVs with acetic acid retains the native conformation of the cytoplasmic domain of band 3 but denatures its transmembrane domain (37). Saturable binding of purified dematin to the alkali-treated IOVs suggests that dematin may not bind to the cytoplasmic domain of band 3 because it is denatured under these conditions. In addition, mild treatment of IOVs with trypsin is known to cleave the cytoplasmic domain of band 3 without any detectable effects on the cytoplasmic domains of glycophorins (38). The inhibition of dematin binding to the trypsin-treated IOVs suggests that dematin is unlikely to bind to the cytoplasmic domains of glycophorins because they are still present on the trypsin-treated IOVs. To resolve this issue, we tested direct binding of purified dematin with the cytoplasmic domain of band 3 that was purified from human erythrocyte ghosts. The cytoplasmic domain of human erythrocyte band 3 was isolated by trypsin digestion of acid-stripped IOVs and further purified by the anion-exchange chromatography as described before (30). Purified cytoplasmic domain of band 3 was incubated with purified dematin, and their binding was measured by the sucrose density gradient centrifugation. No interaction of dematin with the cytoplasmic domain of band 3 was detectable under these conditions. Furthermore, the purified cytoplasmic domain of band 3 failed to displace dematin binding to the alkali-stripped IOVs (data not shown). Together, these results indicate that dematin binds to a trypsin-sensitive site(s) on the cytoplasmic surface of human erythrocyte plasma membrane. Although the identity of this putative membrane protein (receptor) is not yet known, it is unlikely that the cytoplasmic domains of band 3 and glycophorins contribute to the binding of dematin in mature erythrocytes.

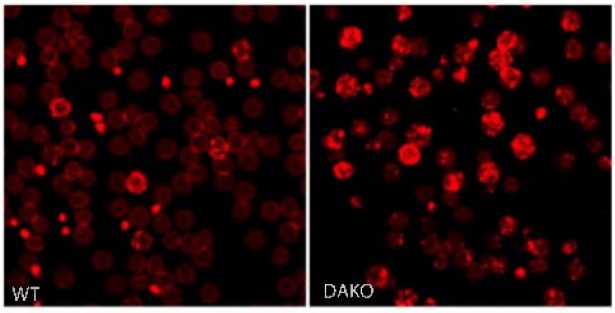

FIGURE 8. **Actin staining of RBC ghosts.** WT and DAKO RBC ghosts were labeled with phalloidin conjugated with Alexa-595 and viewed with a confocal microscope.

DISCUSSION

A major goal of this study was to determine whether the dematin and adducin play similar functional roles in the stabilization and linkage of the junctional complex to the erythrocyte plasma membrane. Stoichiometrically, dematin and adducin are major constituents of the junctional complex, and by virtue of their actin binding and bundling properties, they are believed to regulate the dynamics of actin protofilaments in the erythrocyte membrane (14, 15, 18). Intriguingly, both adducin and dematin have been localized at the junctional complex, and their copy number of ~30,000 (adducin dimers) and ~43,000 (dematin trimers) is consistent with the calculated ~30,000 actin oligomers per erythrocyte (39, 40). Because only mild phenotypes were observed in the individual β-adducin and dematin headpiece knock-out mice, we surmised that dematin and adducin might serve a redundant function at

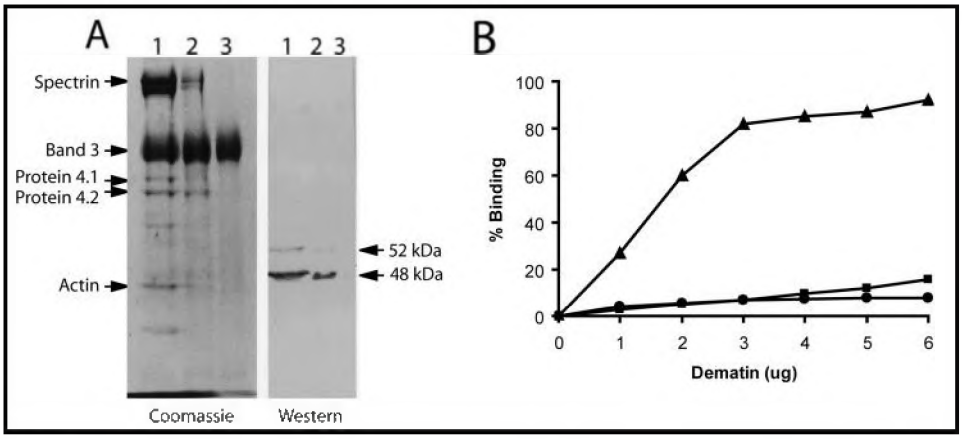

FIGURE 9. **Binding of purified dematin to the stripped inside-out membrane vesicles.** *A*, SDS-PAGE/Coomassie stain and Western blot. *Lane 1*, human erythrocyte ghosts; *lane 2*, spectrin-actin-depleted vesicles extracted by 1.0 M KCl; *lane 3*, spectrin-actin-depleted vesicles extracted at pH 11. *Right panel* shows Western blot analysis of the material shown in *left panel* using an anti-dematin polyclonal antibody. Note that all endogenous dematin was removed from pH 11-extracted vesicles as shown in *lane 3*. *B*, binding of purified dematin to pH 11-extracted vesicles. Membrane vesicles containing bound dematin were recovered by centrifugation and solubilized, and bound dematin was quantified by a quantitative enzyme-linked immunosorbent assay. ●, control, no dematin added; ▲, dematin added to IOVs; ■, dematin added to trypsinized IOVs.

the junctional complex thus ensuring the membrane stability and shape of erythrocytes. The data reported here showing a precipitous decrease in the erythrocyte membrane stability, dramatically reduced life span, and an inability to regulate cell shape in dematin and adducin double knock-out mice are consistent with the functional redundancy of the two proteins at the junctional complex (Figs. 2–4). The near normal composition of major membrane proteins in the DAKO erythrocytes and the increased dissociation of spectrin from the double mutant erythrocyte IOVs suggest that the linkage of the spectrin-actin complex to the plasma membrane may be compromised by the double mutation.

To characterize the mutant erythrocytes, we utilized atomic force microscopy to visualize the differences in membrane topography caused by the double mutation. AFM images showed the presence of large protein aggregates, filamentous cytoskeletal network structure and wide windows through which the underlying cytoplasmic surface of the plasma membrane can be seen. The assignment of topological features follows the example of previous AFM measurements made by Swihart *et al.* (41) from fixed and native human erythrocyte cytoskeleton specimens (41). The authors showed that the plasma membrane sheared free of cytoskeletal components (mainly spectrin) using low ionic solution (5 mM NaP_i, 1 mM EDTA) is a flat surface without any filamentous features. It has a typical thickness (or height relative to the underlying solid substrate) of 4–6 nm, whereas typical membranes with undamaged cytoskeletons still attached are 7–9 nm high, and those with clearly damaged and aggregrated cytoskeleton have height features greater than this and much larger gaps in the network where spectrin has detached from its vertical tether and has aggregated. The height-calibrated AFM images obtained from fixed wild type mouse membrane specimens show three layers of objects positioned at average heights of 3, 6, and 10 nm (Fig. 7). By correspondence to the results from human specimens, these layers are likely to be the plasma membrane, intact cytoskeleton network (and possibly some larger transmembrane components), and aggregated cytoskeletal components, respectively. Another piece of evidence that suggested the intermediate height features are intact spectrin cytoskeleton is their apparent filament length of the fine filament network that corresponds to the intermediate height features that ranges between 20 and 40 nm and is close to EM studies of the spectrin cytoskeleton by Ursitti *et al.* (35). Connected filaments are observed in the WT and DKO mutant specimens but not in the AKO and DAKO specimens. Instead small aggregates appear. Furthermore, fluorescent staining of F-actin in the WT and DAKO erythrocyte membranes revealed relatively larger, denser, and more frequent punctate actin aggregates in the double knock-out erythrocyte ghosts (Fig. 8).

It should be noted that the images shown in Fig. 7 are not intended to be images of perfectly intact membranes. One of the biggest challenges of AFM imaging of biological specimens is avoiding tearing of the specimen as it adheres to the substrate. Weak attachments allow the specimen to detach or wrinkle on the surface, whereas excessively strong attachments can tear the membrane apart. The lectin-coated coverslip presents a large number of relatively weak association bonds with the carbohydrate groups present on the exposed ends of glycophorins, and together provide a relatively secure attachment of the membranes onto the glass coverslip. Because this attachment takes place with intact, unlysed cells, the noncontacting regions of the cell membrane and the cytoskeleton are still available to maintain the cytoplasmic network architecture of the contacting side of the cell as it touches the surface. It is possible that surface forces, which would normally tear the cytoskeleton, can be compensated by the network forces of the intact cell and minimize the damage upon initial contact. Before the shear-induced lysis step, all the cells attached to the coverslip surface are intact and unlysed. Later, some damage and distortion to the cytoskeleton could be seen mainly on the edges of the membrane specimen. Given these considerations, we believe that the major cause of specimen damage occurs during the shear washing step to expose the cytoplasmic interior of the cell, and removal of the intracellular contents and upper membranes before fixation. Fixation before shear lysis is not practical because it also prevents hemolysis, and therefore compromises the exposure of the cytoskeleton, unless even greater mechanical shear is used. In practice, the shear damage can be minimized reproducibly by allowing the fluid to flow imperceptibly across the coverslip, although it is being held at a small angle ($<10°$).

Although the specimen preparation is imperfect, the extent of distortion undergone by the specimen is dependent on its intrinsic resiliency and the strength of its tethering to the underlying plasma membrane, the state of which is preserved by subsequent fixation before imaging. For WT specimens that have the native state of plasma membrane/cytoskeleton interconnections genetically optimized, the least amount of distortion is expected, in contrast to that of the compromised cytoskeleton. For WT mouse specimens, there appears to be more aggregates than was observed in normal human specimens, and this feature may reflect differences in the relative fragility of murine *versus* human erythrocytes in general. Each of the three mutants studied here had relatively greater amount of the cytoskeleton damage. The results can be distinguished into specimens that retained the fine filament network corresponding to intermediate object heights and those that did not. The AKO mutant seems to have retained its fine filament structure even though it has lost a horizontal connection between the cytoskeleton and the plasma membrane via adducin. In contrast, the DKO mutant appears to be missing a specific vertical interaction between the cytoskeleton and the plasma membrane because the intermediate height filament network is lost. These results suggest that multiple vertical stabilizers help to support the spectrin meshwork even if its horizontal connection to the junctional complex is weakened. In the case of DAKO specimens, where both vertical and horizontal associations of the cytoskeleton appear to be broken, the greatest damage was observed as expected.

Despite the loss of two major actin-binding proteins, the overall amount of actin in the DAKO erythrocyte membrane remains essentially unaltered (Fig. 6). This observation implies that the retention of F-actin protofilaments in the erythrocyte plasma membrane is presumably regulated by other cytoskeletal elements. The horizontal stabilization of the F-actin proto-

filaments by protein 4.1, tropomyosin, and tropomodulin could be offered as one mechanism for the retention of F-actin on the plasma membrane. However, the rapid dissociation of spectrin and actin from the DAKO ghosts incubated under low ionic strength conditions argues that the linkage of spectrin-actin junctions to the plasma membrane is significantly weakened by the combined loss of dematin and adducin. This view is consistent with prior evidence showing that the bulk of dematin remains associated with the membrane vesicles when spectrin and actin are removed from the erythrocyte inside-out vesicles (14, 36). In contrast, adducin is quantitatively removed from the erythrocyte inside-out vesicles under similar extraction conditions (20, 42). For dematin to function as a molecular bridge between the junctional complex and the plasma membrane, it must encode a membrane-binding site that is independent of the headpiece domain-mediated interaction with the actin filaments. Indeed, a small amount of the core domain of dematin remains attached to the plasma membrane in the dematin headpiece null mouse erythrocytes (14). To test this possibility directly, we measured binding of purified dematin to erythrocyte inside-out vesicles that are essentially devoid of all major peripheral membrane proteins. Saturable binding of purified dematin to the inside-out vesicles and complete abrogation of this binding by the pretreatment of inside-out vesicles with trypsin suggest that dematin binds to a trypsin-sensitive site on the erythrocyte membrane by a mechanism that is independent of its F-actin binding function. The identity of this putative transmembrane protein that binds to dematin is currently unknown. By using purified cytoplasmic domain of native band 3, our binding and competition studies indicate that band 3 does not block binding of purified dematin to the inside-out vesicles. This observation appears to be consistent with our previous finding that dematin is not altered in the band 3 null mouse erythrocytes, which show a secondary loss of glycophorin A in their plasma membrane (43). Therefore, band 3 and glycophorins are unlikely to serve as the major attachment sites for linking the spectrin-actin junctions to the plasma membrane via dematin. Clearly, the identification of the membrane receptor for dematin will be of paramount importance for future studies, and this information would be invaluable in resolving whether dematin and adducin share the same membrane receptor or link the junctional complex to the plasma membrane via independent receptors.

Acknowledgments—We thank Drs. Toshihiko Hanada for valuable advice and helpful discussions; Hongyu Ni for expert advice on hematology; John Quigley, Richard Labotka, and Ronald Dubreuil for valuable comments on the paper; and members of our research laboratory for critically reviewing the manuscript.

REFERENCES

1. Lux, S. E., and Palek, J. (1995) in *BLOOD: Principles and Practice of Hematology* (Handin, R. I., Lux, S. E., and Stossel, T. P., eds) pp. 1701–1718, J. B. Lippincott, Philadelphia
2. Elgsaeter, A., Stokke, B. T., Mikkelsen, A., and Branton, D. (1986) *Science* **234,** 1217–1223
3. Luna, E. J., and Hitt, A. L. (1992) *Science* **258,** 955–964
4. Chasis, J. A., and Mohandas, N. (1992) *Blood* **80,** 1869–1879
5. Bennett, V. (1989) *Biochim. Biophys. Acta* **988,** 107–121
6. Gilligan, D. M., and Bennett, V. (1993) *Semin. Hematol.* **30,** 74–83
7. Byers, T. J., and Branton, D. (1985) *Proc. Natl. Acad. Sci. U. S. A.* **82,** 6153–6157
8. Eber, S., and Lux, S. E. (2004) *Semin. Hematol.* **41,** 118–141
9. Gallagher, P. G. (2004) *Curr. Hematol. Rep.* **3,** 85–91
10. Derick, L. H., Liu, S. C., Chishti, A. H., and Palek, J. (1992) *Eur. J. Cell Biol.* **57,** 317–320
11. Fowler, V. M. (1996) *Curr. Opin. Cell Biol.* **8,** 86–96
12. Chishti, A. H. (1998) *Curr. Opin. Hematol.* **5,** 116–121
13. Nunomura, W., Takakuwa, Y., Parra, M., Conboy, J., and Mohandas, N. (2000) *J. Biol. Chem.* **275,** 24540–24546
14. Khanna, R., Chang, S. H., Andrabi, S., Azam, M., Kim, A., Rivera, A., Brugnara, C., Low, P. S., Liu, S. C., and Chishti, A. H. (2002) *Proc. Natl. Acad. Sci. U. S. A.* **99,** 6637–6642
15. Joshi, R., Gilligan, D. M., Otto, E., McLaughlin, T., and Bennett, V. (1991) *J. Cell Biol.* **115,** 665–675
16. Gardner, K., and Bennett, V. (1987) *Nature* **328,** 359–362
17. Kuhlman, P. A., Hughes, C. A., Bennett, V., and Fowler, V. M. (1996) *J. Biol. Chem.* **271,** 7986–7991
18. Mische, S. M., Mooseker, M. S., and Morrow, J. S. (1987) *J. Cell Biol.* **105,** 2837–2845
19. Azim, A. C., Knoll, J. H., Beggs, A. H., and Chishti, A. H. (1995) *J. Biol. Chem.* **270,** 17407–17413
20. Gardner, K., and Bennett, V. (1986) *J. Biol. Chem.* **261,** 1339–1348
21. Scaramuzzino, D. A., and Morrow, J. S. (1993) *Proc. Natl. Acad. Sci. U. S. A.* **90,** 3398–3402
22. Cohen, C. M., and Gascard, P. (1992) *Semin. Hematol.* **29,** 244–292
23. Muro, A. F., Marro, M. L., Gajovic, S., Porro, F., Luzzatto, L., and Baralle, F. E. (2000) *Blood* **95,** 3978–3985
24. Gilligan, D. M., Lozovatsky, L., Gwynn, B., Brugnara, C., Mohandas, N., and Peters, L. L. (1999) *Proc. Natl. Acad. Sci. U. S. A.* **96,** 10717–10722
25. Peters, L. L., Birkenmeier, C. S., and Barker, J. E. (1992) *Blood* **80,** 2122–2127
26. Laemmli, U. K. (1970) *Nature* **227,** 680–685
27. Liu, F., Burgess, J., Mizukami, H., and Ostafin, A. (2003) *Cell Biochem. Biophys.* **38,** 251–270
28. Liu, F., Mizukami, H., Sarnaik, S., and Ostafin, A. (2005) *J. Struct. Biol.* **150,** 200–210
29. Chishti, A., Faquin, W., Wu, C. C., and Branton, D. (1989) *J. Biol. Chem.* **264,** 8985–8991
30. Korsgren, C., and Cohen, C. M. (1986) *J. Biol. Chem.* **261,** 5536–5543
31. Chishti, A., Levin, A., and Branton, D. (1988) *Nature* **334,** 718–721
32. Bradford, M. M. (1976) *Anal. Biochem.* **72,** 248–254
33. Peters, L. L., Shivdasani, R. A., Liu, S. C., Hanspal, M., John, K. M., Gonzalez, J. M., Brugnara, C., Gwynn, B., Mohandas, N., Alper, S. L., Orkin, S. H., and Lux, S. E. (1996) *Cell* **86,** 917–927
34. Southgate, C. D., Chishti, A. H., Mitchell, B., Yi, S. J., and Palek, J. (1996) *Nat. Genet.* **14,** 227–230
35. Ursitti, J. A., Pumplin, D. W., Wade, J. B., and Bloch, R. J. (1991) *Cell Motil. Cytoskeleton* **19,** 227–243
36. Siegel, D. L., and Branton, D. (1985) *J. Cell Biol.* **100,** 775–785
37. Appell, K. C., and Low, P. S. (1982) *Biochemistry* **21,** 2151–2157
38. Steck, T. L., Ramos, B., and Strapazon, E. (1976) *Biochemistry* **15,** 1153–1161
39. Shen, B. W., Josephs, R., and Steck, T. L. (1986) *J. Cell Biol.* **102,** 997–1006
40. Lin, D. C., and Lin, S. (1978) *J. Biol. Chem.* **253,** 1415–1419
41. Swihart, A. H., Mikrut, J. M., Ketterson, J. B., and Macdonald, R. C. (2001) *J. Microsc. (Oxf)* **204,** 212–225
42. Matsuoka, Y., Li, X., and Bennett, V. (2000) *Cell. Mol. Life Sci.* **57,** 884–895
43. Hassoun, H., Hanada, T., Lutchman, M., Sahr, K. E., Palek, J., Hanspal, M., and Chishti, A. H. (1998) *Blood* **91,** 2146–2151